

Computing entanglement entropy of interacting fermions with quantum Monte Carlo: Why we failed and how to get it right

Gaopei Pan,^{1,2,*} Yuan Da Liao,^{3,4,†} Weilun Jiang,^{1,2} Jonathan D’Emidio,⁵ Yang Qi,^{3,4,6} and Zi Yang Meng^{7,‡}

¹*Beijing National Laboratory for Condensed Matter Physics and Institute of Physics,
Chinese Academy of Sciences, Beijing 100190, China*

²*School of Physical Sciences, University of Chinese Academy of Sciences, Beijing 100049, China*

³*State Key Laboratory of Surface Physics, Fudan University, Shanghai 200438, China*

⁴*Center for Field Theory and Particle Physics, Department of Physics, Fudan University, Shanghai 200433, China*

⁵*Donostia International Physics Center, P. Manuel de Lardizabal 4, 20018 Donostia-San Sebastián, Spain*

⁶*Collaborative Innovation Center of Advanced Microstructures, Nanjing 210093, China*

⁷*Department of Physics and HKU-UCAS Joint Institute of Theoretical and Computational Physics,
The University of Hong Kong, Pokfulam Road, Hong Kong SAR, China*

(Dated: April 4, 2023)

There is no doubt that the information hidden in quantum entanglement can be used to infer the organizing principle of various quantum phases of matter, ranging from spontaneous symmetry breaking phases, quantum critical points to topologically ordered states. It is far from clear, however, whether entanglement measures, such as the entanglement entropy (EE), can actually be obtained with the precision required to observe these subtle features – usually in the form of universal finite size scaling behavior – in highly entangled quantum matter. In the case of 2D interacting fermionic lattice models with gapless spectra, such as in the Hubbard model, the computation of the EE has faced severe limitations, making reliable data in the universal scaling regime off limits to all existing numerical algorithms. Here we explain the reason for the previously unsuccessful attempts in EE computations in quantum Monte Carlo simulations and more importantly, show how to overcome the conceptual and computational barrier with the incremental algorithm [1, 2], such that the computation of the EE in 2D interacting fermion systems finally becomes easy and reliable.

Introduction.— The entanglement entropy (EE) of free fermion systems can be derived via the Widom-Sobolev formula [3–6] and results in the $L \log(L)$ scaling of a free Fermi surface in 2D [7–12]. The universal log-coefficient beyond the area law scaling for free Dirac fermions has also been obtained [12–16]. On the contrary, the computation of the EE for interacting fermion lattice models in 2D has been rare, with notable exceptions including topological EE computed from fractional quantum Hall groundstates [17, 18].

In the world of auxiliary-field determinant quantum Monte Carlo (DQMC) simulations, significant algorithmic advances in the computation of Rényi EE have been made. This was spearheaded by the original work of Grover [19] who used the free fermion decomposition of the reduced density matrix to identify an estimator based on independent auxiliary-field configurations. Despite its elegance, early implementations of this approach revealed severe statistical errors at strong coupling and not-even-large subsystem sizes [20, 21]. This motivated translating the highly successful replica approach from path-integral spin systems [22] into the auxiliary-field fermion language [23–25], which however proved cumbersome since it required introducing a replicated environment for the entangling subsystem (effectively increasing the total system size) and using an imaginary-time dependent Hamiltonian, thus substantially increasing the computation burden (the computational complexity of standard DQMC already scales as $O(\beta N^3)$ with $\beta = \frac{1}{T}$ the inverse temperature and $N = L^d$ for d spatial dimen-

sion systems with linear size L). Furthermore it suffered from subtle stability issues regarding the computation of Green’s functions. In the end, all attempts thus far in computing Rényi EE for interacting fermions in 2D have not achieved the precision required to resolve, for instance in the simplest example, an area law plus universal log [26] due to Goldstone modes in the square lattice Hubbard model.

On the other hand, since the QMC computational complexity in spin/boson systems scales as $O(\beta N)$, the EE of 2D Heisenberg models [22, 27–30] and other related systems [31, 32] have had much success, although the data quality is always a serious issue for extracting the expected universal scaling coefficients. This problem is completely solved by the introduction of the *incremental* algorithm [33–36], which converts the computation of the Rényi EE into the parallel execution of the Jarzynski equality [37] of the free energy difference between partition functions on replicated manifolds, making the precise determination of EE scaling on various 2D quantum spin models possible with exquisite data quality, and controlled results with the expected CFT information can then be obtained, including in the Néel phase of antiferromagnetic Heisenberg model, at the (2+1)D $O(3)$ quantum critical point, the deconfined quantum critical point and inside the Z_2 topological ordered Kagome quantum spin liquid [34–36], to name a few.

It is in the process of developing the *incremental* algorithm into DQMC for the entanglement computation in interacting fermion systems [1], that we understand

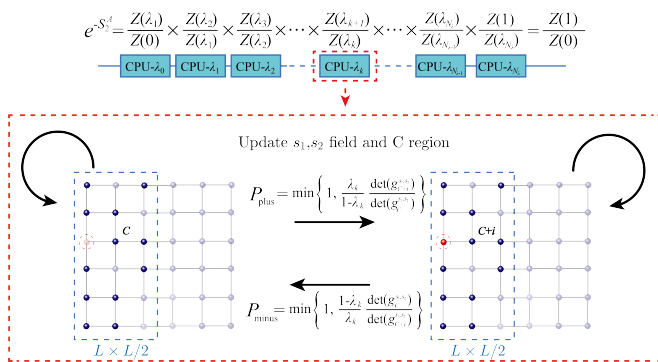


FIG. 1. **The incremental computation of EE.** The entanglement region A is denoted as the blue dashed box. As in Eq. (4), we split the computation of the ratio into the parallel execution of many ratios, where each ratio is bounded with a scale of unity and the sites inside A for each parallel piece are not fixed but changes stochastically. The adding and removing site (denoted as the red dot and dashed circle) in A are carried out with probabilities P_{plus} and P_{minus} . The QMC updates of the auxiliary field for each parallel piece are carried out independently. When update the $s_{1,2}$ field, the sites in A and in the environment are fixed, as denoted by the circular arrows.

the reason why the original *direct* implementation of the EE computation [19–21, 23–25, 38] does not work – not because of the heavy-duty computation added to the already expensive DQMC by adding replicas, but because the direct computation does not use the correct sampling weight to construct a proper Markov chain Monte Carlo simulation. The incremental algorithm [1, 2], on the other hand, features two key improvements:

1. designing the effective Monte Carlo importance sampling weight for EE computations and
2. conditioning the exponentially small partition function ratio into a parallel execution of values with scales of unity

and consequently offers the correct scheme that can be utilized to extract the EE with reliable data quality and controllable polynomial computation complexity. In this paper, we use the prototypical example of 2D interacting fermion lattice models – the square lattice Hubbard model – to fully explain the simple but fundamental difference between the previous *direct* and the improved *incremental* computation of EE and to establish the correct protocol for entanglement computation in interacting fermionic lattice models.

Model and Method.— We study the 2nd Rényi EE for the square lattice Hubbard model at half-filling, with the Hamiltonian

$$H = -t \sum_{\langle i,j \rangle} (c_{i,\sigma}^\dagger c_{j,\sigma} + h.c.) + U \sum_i (n_{i,\uparrow} + n_{i,\downarrow} - 1)^2, \quad (1)$$

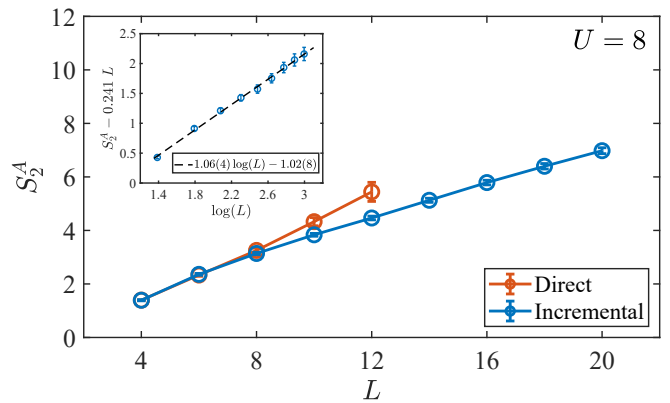


FIG. 2. **The EE of square lattice Hubbard model at $U = 8$.** The entanglement region A is of size $L \times L/2$. The red and blue lines are from the direct and incremental methods, respectively. The deviation of the direct computation for $L \geq 8$ is obvious. The inset shows the incremental data of $S_2^A - 0.241L$ versus $\log(L)$, with the slope (denoted as the black dashed line) representing the universal log-coefficient $s = \frac{N_G}{2} = 1$ in Eq. (3), our fitting results of $s = 1.06(4)$ is fully consistent with expected behavior of Néel antiferromagnetic Mott insulator with $N_G = 2$. It is important to note that the errorbars of direct data (red dots) are not credible, because they didn't converge, as shown in Fig. 4.

where $c_{i,\sigma}^\dagger$ and $c_{i,\sigma}$ denote the creation and annihilation operators with spin $\sigma = \uparrow, \downarrow$ on site i , $\langle i, j \rangle$ represents the nearest neighbor hopping, $n_{i,\sigma} = c_{i,\sigma}^\dagger c_{i,\sigma}$ is the particle number operator for spin σ , and U/t tunes the onsite interaction strength, with $t = 1$ the energy unit.

Since the Rényi EE is a ground-state property of a quantum system, we utilize the projector DQMC method. As described in the Supplemental Material (SM) [39] and relevant literature [40–46], it carries out a Hubbard-Stratonovich transformation to introduce an auxiliary field $\{s\}$ to decouple the quartic fermion interaction and compute ground-state observable O as $\langle O \rangle = \frac{\sum_{\{s\}} W^s(O)^s}{\sum_{\{s\}} W^s}$, where W^s is the unnormalized weight of configuration s proportional to a determinant whose elements depends on s [39]. As shown in Ref. [19], to calculate the Rényi EE of interacting fermions in DQMC, Grover introduced a *direct* formula based on the free fermion decomposition of the reduced density matrix ρ_A (with entangling region A) using two independent auxiliary field replicas, such that the 2nd Rényi EE S_2^A is given by

$$e^{-S_2^A} = \frac{Z(1)}{Z(0)} := \frac{\sum_{\{s_1, s_2\}} \mathbf{W}^{s_1, s_2} \det g_A^{s_1, s_2}}{\sum_{\{s_1, s_2\}} \mathbf{W}^{s_1, s_2}}, \quad (2)$$

where $\mathbf{W}^{s_1, s_2} = W^{s_1} W^{s_2}$, $g_A^{s_1, s_2} = G_A^{s_1} G_A^{s_2} + (\mathbb{I} - G_A^{s_1})(\mathbb{I} - G_A^{s_2})$ is the Grover matrix connecting the Green's functions G^{s_1} and G^{s_2} of the two replicas on A . $Z(1)$ stands for the partition function with the fully con-

nected entangling region between the two replicas and $Z(0)$ the partition function of two independent replicas, we use $\lambda \in [0, 1]$ to parametrize the evolution from $Z(\lambda = 0)$ to $Z(\lambda = 1)$.

Based on Eq. (2), one can compute the S_2^A as in conventional DQMC simulations with the configurational weights \mathbf{W}^{s_1, s_2} , and this is indeed what has been implemented in previous attempts [19–21]. But it was noticed that the obtained EE suffered greatly from numerical instability issue with poor data quality that they cannot be used to extract the universal scaling behavior

$$S_2^A(L) = aL \log L + bL + s \log L + c \quad (3)$$

where the coefficients a stems from the 2D Fermi surface and can be derived at the non-interacting limit [3, 7–12] (see Eq. (S7) and Fig. S1), b governs the area law scaling and s is the universal corner contributions at critical points [13, 32, 47], or is proportional to the number of goldstone modes in symmetry broken phases [26]. For example, for Eq. (1) at $U = 8$, the $s = \frac{N_G}{2} = 1$ where $N_G = 2$ is the number of Goldstone modes for a Néel state (see Fig. 2 below), a result that has eluded implementations using the direct approach of Grover.

What has been seen, however, is that for slightly larger system sizes ($L \geq 8$) and slightly stronger interactions ($U \geq 4$), the distribution of the Grover determinants became very broad with spikes (rare events). As will show below, we find if one insists on direct computation of EE with Eq. (2), it is these rare events that actually make great contributions to the expectation value of EE, but since they occur less often with respect to the L and U , one will certainly run into problem when trying to obtain the controlled finite size scaling behavior of EE as a function of L and U . This is the signature, that points out the *direct* computation of EE in Eq. (2) actually follows the incorrect distribution \mathbf{W}^{s_1, s_2} , and consequently does not average according to the important sampling of a good Markov chain Monte Carlo process.

To address this issue, i.e. to sample properly in the replicated configurational space of the EE computation, the incremental algorithm for fermions was recently developed in Ref. [1] and further applied in Ref. [2]. As discussed in the introduction and sketched in Fig. 1, the incremental algorithm has improved the direct computation in two main points:

First, it introduces a new auxiliary sampling configuration, namely the subset C of the entanglement region A , which, instead of calculating $e^{-S_2^A}$ directly, converts the computation of $e^{-S_2^A}$ into a parallel execution of incremental ratios as

$$e^{-S_2^A} = \frac{Z(1)}{Z(0)} := \frac{Z(\lambda_1)}{Z(0)} \frac{Z(\lambda_2)}{Z(\lambda_1)} \dots \frac{Z(\lambda_{k+1})}{Z(\lambda_k)} \dots \frac{Z(1)}{Z(\lambda_{N_\lambda})}, \quad (4)$$

where $Z(\lambda) = \sum_{C \subseteq A} \lambda^{N_C} (1 - \lambda)^{N_A - N_C} Z_C$ [1, 34] with $\lambda \in [0, 1]$, N_C (N_A) is the number of site in region C

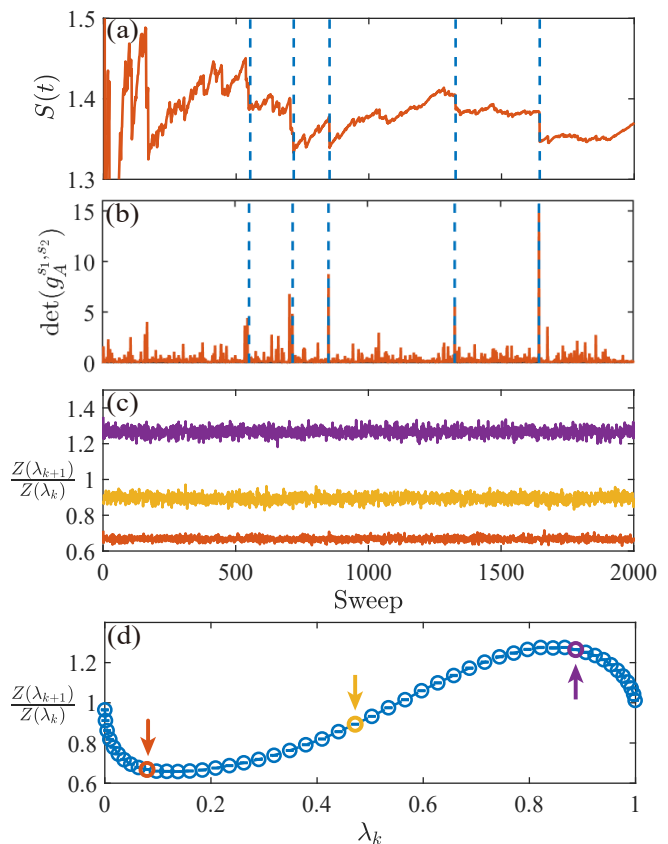


FIG. 3. **Difference between direct and incremental measurements.** (a) and (b) show the time series of $\det(g_A^{s_1, s_2})$ and $S(t)$ from a single Markov chain using direct method with $U = 8, L = 4$. Both observables are clearly not normal distributed and the rare events in the form of the sudden drop in (a) and spikes in (b), denoted by blue dotted lines, are clearly seen. (c) and (d) $\frac{Z(\lambda_{k+1})}{Z(\lambda_k)}$ for $U = 8, L = 10$ by incremental method with $\lambda \in [0, 1]$. The number of λ_k is 50. As discussed in the main text, around Eqs. (4) and (5), each piece has the value of scale unity. The three arrows in panel(d) point out the position of three different λ_k values where the time series are shown on in panel(c). The observables are now normal distributed.

(A) and $Z_C = \sum_{\{s_1\}, \{s_2\}} \mathbf{W}^{s_1, s_2} \det g_C^{s_1, s_2}$. More importantly, $\frac{Z(\lambda_{k+1})}{Z(\lambda_k)}$ is computed as

$$\frac{Z(\lambda_{k+1})}{Z(\lambda_k)} = \frac{\sum_{\{s_1, s_2, C \subseteq A\}} \mathbf{W}_C^{s_1, s_2}(\lambda_k) O_C(\lambda_k, \lambda_{k+1})}{\sum_{\{s_1, s_2, C \subseteq A\}} \mathbf{W}_C^{s_1, s_2}(\lambda_k)}, \quad (5)$$

where the effective observable for the EE is

$$O_C(\lambda_k, \lambda_{k+1}) = \left(\frac{\lambda_{k+1}}{\lambda_k} \right)^{N_C} \left(\frac{1 - \lambda_{k+1}}{1 - \lambda_k} \right)^{N_A - N_C}, \quad (6)$$

and the effective sampling weight of the EE computation is

$$\mathbf{W}_C^{s_1, s_2}(\lambda_k) = \lambda_k^{N_C} (1 - \lambda_k)^{N_A - N_C} \mathbf{W}^{s_1, s_2} \det g_C^{s_1, s_2}. \quad (7)$$

We note the weight ratio $\frac{W_C^{s'_1, s_2}(\lambda_k)}{W_C^{s_1, s_2}(\lambda_k)} = \frac{W^{s'_1} \det g_C^{s'_1, s_2}}{W^{s_1} \det g_C^{s_1, s_2}}$ of incremental sampling in Eq. (5) is explicitly different from that of direct sampling $\frac{W^{s'_1, s_2}}{W^{s_1, s_2}} = \frac{W^{s'_1}}{W^{s_1}}$ in Eq. (2), in that it contains the contribution from determinant of Grover matrix. In addition, the incremental method updates the configurations C stochastically with probabilities $P_{\text{plus}} = \frac{\lambda_k}{1-\lambda_k} \frac{\det(g_C^{s_1, s_2})}{\det(g_C^{s'_1, s_2})}$ and $P_{\text{minus}} = \frac{1-\lambda_k}{\lambda_k} \frac{\det(g_C^{s_1, s_2})}{\det(g_C^{s'_1, s_2})}$ for adding or moving one site from region C , as shown in Fig. 1. When sampling according to Eq. (7), there will be no spikes in the observable $O_C(\lambda_k, \lambda_{k+1})$, provided λ_k and λ_{k+1} are close enough such that their histograms of N_C overlap. The ensemble average can then be properly carried out.

Second, we find each piece of the ratio $\frac{Z(\lambda_{k+1})}{Z(\lambda_k)}$ in Eq. (4) can be computed independently, which means massive parallelization of the high-performance computation (denoted in the upper panel of Fig. 1) can greatly reduce the computation time. Moreover, although the $e^{-S_2^A}$ is eventually an exponentially small quantity, each piece in the product of Eq. (4) actually has well-behaved bound of the scale of unity, since the independent computation of the $\frac{Z(\lambda_{k+1})}{Z(\lambda_k)}$ is very well-behaved, their product gives rise to the controlled EE with the same polynomial complexity as DQMC itself. The increments $\frac{Z(\lambda_{k+1})}{Z(\lambda_k)}$ of $O(1)$ and their histograms in the non-interacting case for $U = 0$ and $L = 4$ are also shown in Fig. S2 in the SM [39].

It is these two major improvements of incremental over the direct computation of EE, that one can now access the universal entanglement scaling behavior of 2D interacting fermion models, as we now turn to.

Results in 2D Hubbard model.— We have carried out the EE computation for square lattice Hubbard model with $L = 4, 8, 10, 12, 16, 20$. Most of our data are obtained at $U = 8$ where the system is in antiferromagnetic Mott insulator state.

The $U = 0$ limit is discussed in the SM [39], where the computed $aL \log L$ with the coefficient $a = \frac{1}{2}$ in Eq. (3) obtained in full agreement with the analytic expectation from the Widom-Sobolev formula [3–7, 12].

With the free Fermi surface limit under control, we then compute the EE at $U = 8$ calculated by these two methods, the results are shown in Fig. 2. Here the entanglement region is half of the lattice: $L/2 \times L$. One clearly sees that when the system size L is small, the results of the two methods coincide, but when the size gradually increases, the mean value of the direct method starts to deviate from the expected behavior of the incremental one.

Moreover, since the half-filled square lattice Hubbard is always in an antiferromagnetic Mott insulating phase ($U > 0$), the S_2^A of the system with spontaneous broken $SU(2)$ continuous symmetry should have a form in Eq. (3) with $a = 0$, b finite and the universal log-

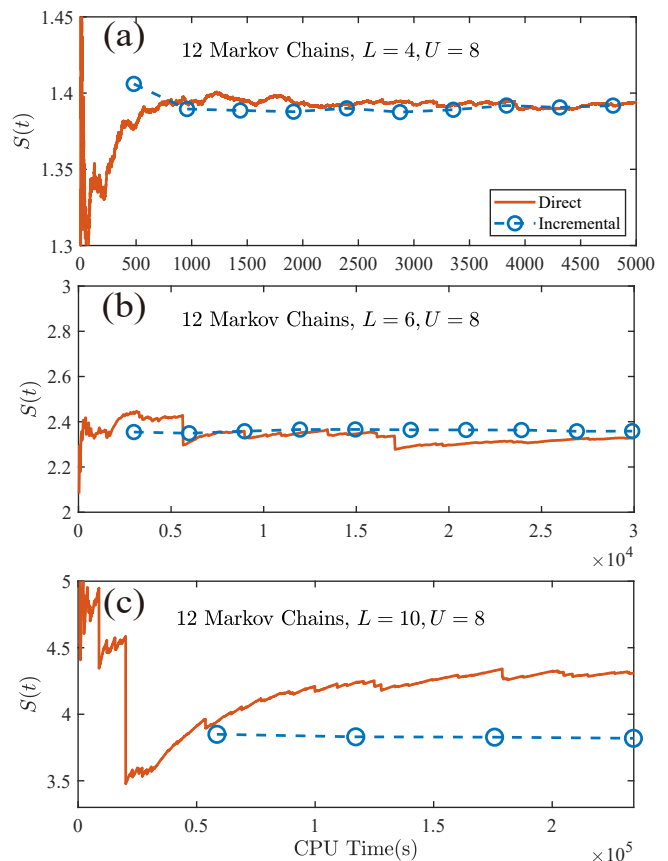


FIG. 4. **Convergence comparison between the direct and the incremental methods.** (a) For $L = 4, U = 8$, the direct method (red line) can slowly converge to exact value while the blue dots, the incremental method converges very fast. (b) For $L = 6, U = 8$, the direct method converge within a reasonable CPU time but with big fluctuations, while the incremental method still converges. (c) For $L = 10, U = 8$, the direct method cannot converge within the reasonable CPU time, but the incremental method still converges.

coefficient $s = \frac{N_G}{2} = 1$ where $N_G = 2$ is the number of the Goldstone modes [26, 32]. As shown in the inset of Fig. 2, the log-coefficient after extracting the area law term is $1.06(4)$, well consistent with the theoretical expected value 1. The results of the direct computation will not be able to perform such analysis.

To reveal the difference of the two methods, we record the time series of EE computation along the Markov chain, $S(t) = -\log\left(\frac{1}{t} \sum_{i=1}^t e^{-S_2^A(i)}\right)$, where $S(t)$ represents the expectation value of observable S_2^A after first t DQMC sweeps. As shown in Fig. 3(b), for the direct method, S_2^A does not follow normal distribution, and whenever a peak is sampled, there is an obvious drop in the mean value of EE calculated, as shown in Fig. 3(a). The $S(t)$ is affected by these rare events, which renders the direct computation with very poor performance. Due to these rare events, when the L and U are at medium to

large values, a very long Markov chain is needed to obtain accurate values, as shown in Fig. 3(b) and red lines in Fig. 4(a), (b), (c). In fact, from Fig. 4 (c), one sees for $L = 10$ and $U = 8$, the direct $S(t)$ has not converged.

The incremental EE does not have such problem. For each piece of parallel computation, the range of the observable is controlled, and we have already considered the determinant of the Grover matrix in the weight during sampling, i.e Eq. (7), so even if not many samples are taken, the deviation from the accurate value will not be too large. In Fig. 3(d), the range of the partition function ratios is given, with $L = 10, U = 8$ and $\lambda_k = \left[\sin \frac{(0.002+50(k-1))\pi}{2} \right]^2$. The number of λ_k is 50. And the sampling distributions of three colored points are selected as examples and shown in Fig. 3(c). Based on these advantages, the incremental method with its fast convergence and parallel computation, clearly outperform the direction computation. As shown in Fig. 4, for $L = 4, U = 8$, the direct method was still able to converge to the exact value, but when the size goes up to $L = 10$, the direct method converged slowly and the incremental method still performed well.

Discussion.— Overall, we clarify the decade long mystery of not being able to obtain the EE in 2D interacting fermion models. By utilizing the square lattice Hubbard model, we reveal the fundamental difference between the *direct* and *incremental* computation of EE in that, the two major improvements are i). designing the effective Monte Carlo sampling weight and ii). conditioning the exponential factor of partition function ratios into parallel execution of values with scale of unity. This bestows the incremental method the robust and accurate access of the entanglement scaling behavior of 2D interacting fermion models. We believe our approach establishes the correct practice of the EE computation for many highly entangled fermion quantum matter such as the quantum critical metal and non-Fermi-liquid [12, 44–46, 48–54], the fermion deconfined quantum critical point [2, 16, 55, 56] and the correlated flat-band Moiré materials [57, 58] and kagome metals [59, 60].

Acknowledgments— We thank Jiarui Zhao, Zheng Yan for collaborations on incremental algorithm for spin/boson systems [35, 36] and inspiring discussions on the related topic. We thank Fakher Assaad for bringing our attention to the instability issue of EE computation over the years. GPP, WLJ and ZYM acknowledge support from the RGC of Hong Kong SAR of China (Project Nos. 17301420, 17301721, AoE/P-701/20, 17309822, HKU C7037-22G), the ANR/RGC Joint Research Scheme sponsored by Research Grants Council of Hong Kong SAR of China and French National Reserach Agency (Project No. A-HKU703/22). YDL acknowledges support from National Natural Science Foundation of China (Grant No. 12247114) and the China Postdoctoral Science Foundation (Grants Nos.

2021M700857 and 2021TQ0076).

* gppan@iphy.ac.cn

† ydliao@fudan.edu.cn

‡ zymeng@hku.hk

- [1] J. d’Emidio, R. Orus, N. Laflorencie, and F. de Juan, arXiv preprint arXiv:2211.04334 (2022).
- [2] Y. Da Liao, G. Pan, W. Jiang, Y. Qi, and Z. Y. Meng, arXiv e-prints, arXiv:2302.11742 (2023), arXiv:2302.11742 [cond-mat.str-el].
- [3] D. Gioev and I. Klich, Phys. Rev. Lett. **96**, 100503 (2006).
- [4] H. Leschke, A. V. Sobolev, and W. Spitzer, Phys. Rev. Lett. **112**, 160403 (2014).
- [5] A. V. Sobolev, Journal of Functional Analysis **266**, 5886 (2014).
- [6] A. V. Sobolev, Integral Equations and Operator Theory **81**, 435 (2015).
- [7] B. Swingle, Phys. Rev. Lett. **105**, 050502 (2010).
- [8] R. Helling, H. Leschke, and W. Spitzer, International Mathematics Research Notices **2011**, 1451 (2010).
- [9] M. Cramer, J. Eisert, and M. B. Plenio, Phys. Rev. Lett. **98**, 220603 (2007).
- [10] T. Barthel, M.-C. Chung, and U. Schollwöck, Phys. Rev. A **74**, 022329 (2006).
- [11] R. V. Mishmash and O. I. Motrunich, Phys. Rev. B **94**, 081110 (2016).
- [12] W. Jiang, B.-B. Chen, Z. H. Liu, J. Rong, F. F. Assaad, M. Cheng, K. Sun, and Z. Y. Meng, arXiv e-prints, arXiv:2209.07103 (2022), arXiv:2209.07103 [cond-mat.str-el].
- [13] H. Casini and M. Huerta, Nuclear Physics B **764**, 183 (2007).
- [14] S. Sahoo, E. M. Stoudenmire, J.-M. Stéphan, T. Devakul, R. R. P. Singh, and R. G. Melko, Phys. Rev. B **93**, 085120 (2016).
- [15] J. Helmes, L. E. Hayward Sierens, A. Chandran, W. Witczak-Krempa, and R. G. Melko, Phys. Rev. B **94**, 125142 (2016).
- [16] Z. H. Liu, W. Jiang, B.-B. Chen, J. Rong, M. Cheng, K. Sun, Z. Y. Meng, and F. F. Assaad, arXiv e-prints, arXiv:2212.11821 (2022), arXiv:2212.11821 [cond-mat.str-el].
- [17] M. P. Zaletel, R. S. K. Mong, and F. Pollmann, Phys. Rev. Lett. **110**, 236801 (2013).
- [18] W. Zhu, S. S. Gong, F. D. M. Haldane, and D. N. Sheng, Phys. Rev. Lett. **115**, 126805 (2015).
- [19] T. Grover, Phys. Rev. Lett. **111**, 130402 (2013).
- [20] F. F. Assaad, T. C. Lang, and F. Parisen Toldin, Phys. Rev. B **89**, 125121 (2014).
- [21] C.-C. Chang, R. R. P. Singh, and R. T. Scalettar, Phys. Rev. B **90**, 155113 (2014).
- [22] M. B. Hastings, I. González, A. B. Kallin, and R. G. Melko, Phys. Rev. Lett. **104**, 157201 (2010).
- [23] P. Broecker and S. Trebst, Journal of Statistical Mechanics: Theory and Experiment **2014**, P08015 (2014).
- [24] F. F. Assaad, Phys. Rev. B **91**, 125146 (2015).
- [25] P. Broecker and S. Trebst, Phys. Rev. E **94**, 063306 (2016).
- [26] M. A. Metlitski and T. Grover, arXiv preprint

- arXiv:1112.5166 (2011).
- [27] A. B. Kallin, M. B. Hastings, R. G. Melko, and R. R. P. Singh, *Phys. Rev. B* **84**, 165134 (2011).
- [28] S. Humeniuk and T. Roscilde, *Phys. Rev. B* **86**, 235116 (2012).
- [29] J. Helmes and S. Wessel, *Phys. Rev. B* **89**, 245120 (2014).
- [30] B. Kulchytskyi, C. M. Herdman, S. Inglis, and R. G. Melko, *Phys. Rev. B* **92**, 115146 (2015).
- [31] S. V. Isakov, M. B. Hastings, and R. G. Melko, *Nature Physics* **7**, 772 (2011).
- [32] N. Laflorencie, *Physics Reports* **646**, 1 (2016).
- [33] V. Alba, *Phys. Rev. E* **95**, 062132 (2017).
- [34] J. D’Emidio, *Phys. Rev. Lett.* **124**, 110602 (2020).
- [35] J. Zhao, B.-B. Chen, Y.-C. Wang, Z. Yan, M. Cheng, and Z. Y. Meng, *npj Quantum Materials* **7**, 1 (2022).
- [36] J. Zhao, Y.-C. Wang, Z. Yan, M. Cheng, and Z. Y. Meng, *Phys. Rev. Lett.* **128**, 010601 (2022).
- [37] C. Jarzynski, *Phys. Rev. Lett.* **78**, 2690 (1997).
- [38] F. Parisen Toldin and F. F. Assaad, *Phys. Rev. Lett.* **121**, 200602 (2018).
- [39] In this Supplementary Material, we discuss in detail the projector DQMC algorithm and the implementation of the incremental algorithm for EE computation therein. We also provide the exact results of the EE at the non-interacting limits.
- [40] F. Assaad and H. Evertz, in *Computational Many-Particle Physics*, Vol. 739, edited by H. Fehske, R. Schneider, and A. Weiße (Springer Berlin Heidelberg, Berlin, Heidelberg, 2008) pp. 277–356.
- [41] X. Y. Xu, Y. Qi, L. Zhang, F. F. Assaad, C. Xu, and Z. Y. Meng, *Phys. Rev. X* **9**, 021022 (2019).
- [42] Y. Da Liao, Z. Y. Meng, and X. Y. Xu, *Physical Review Letters* **123**, 157601 (2019).
- [43] Yuan Da Liao, Jian Kang, Clara N. Breiø, Xiao Yan Xu, Han-Qing Wu, Brian M. Andersen, Rafael M. Fernandes, and Zi Yang Meng, *Physical Review X* **11**, 011014 (2021).
- [44] Y. Da Liao, X. Y. Xu, Z. Y. Meng, and Y. Qi, *Phys. Rev. B* **106**, 075111 (2022).
- [45] Y. Da Liao, X. Y. Xu, Z. Y. Meng, and Y. Qi, *Phys. Rev. B* **106**, 115149 (2022).
- [46] Y. Da Liao, X. Y. Xu, Z. Y. Meng, and Y. Qi, *Phys. Rev. B* **106**, 155159 (2022).
- [47] E. Fradkin and J. E. Moore, *Phys. Rev. Lett.* **97**, 050404 (2006).
- [48] X. Y. Xu, Z. H. Liu, G. Pan, Y. Qi, K. Sun, and Z. Y. Meng, *Journal of Physics: Condensed Matter* **31**, 463001 (2019).
- [49] Z. H. Liu, G. Pan, X. Y. Xu, K. Sun, and Z. Y. Meng, *Proceedings of the National Academy of Sciences* **116**, 16760 (2019).
- [50] G. Pan, W. Jiang, and Z. Y. Meng, *Chinese Physics B* **31**, 127101 (2022).
- [51] X. Y. Xu, K. Sun, Y. Schattner, E. Berg, and Z. Y. Meng, *Phys. Rev. X* **7**, 031058 (2017).
- [52] A. A. Patel, H. Guo, I. Esterlis, and S. Sachdev, arXiv e-prints, arXiv:2203.04990 (2022), arXiv:2203.04990 [cond-mat.str-el].
- [53] I. Esterlis, H. Guo, A. A. Patel, and S. Sachdev, *Phys. Rev. B* **103**, 235129 (2021).
- [54] P. Lunts, M. S. Albergo, and M. Lindsey, arXiv e-prints, arXiv:2204.14241 (2022), arXiv:2204.14241 [cond-mat.str-el].
- [55] M. Christos, Z.-X. Luo, H. Shackleton, M. Scheurer, and S. Sachdev, arXiv e-prints, arXiv:2302.07885 (2023), arXiv:2302.07885 [cond-mat.str-el].
- [56] Y. Liu, Z. Wang, T. Sato, M. Hohenadler, C. Wang, W. Guo, and F. F. Assaad, *Nature communications* **10**, 1 (2019).
- [57] G. Pan, X. Zhang, H. Lu, H. Li, B.-B. Chen, K. Sun, and Z. Y. Meng, *Phys. Rev. Lett.* **130**, 016401 (2023).
- [58] X. Zhang, G. Pan, B.-B. Chen, H. Li, K. Sun, and Z. Y. Meng, arXiv e-prints, arXiv:2210.11733 (2022), arXiv:2210.11733 [cond-mat.str-el].
- [59] J.-X. Yin, B. Lian, and M. Z. Hasan, *Nature* **612**, 647 (2022).
- [60] M. Kang, L. Ye, S. Fang, J.-S. You, A. Levitan, M. Han, J. I. Facio, C. Jozwiak, A. Bostwick, E. Rotenberg, M. K. Chan, R. D. McDonald, D. Graf, K. Kaznatcheev, E. Vescovo, D. C. Bell, E. Kaxiras, J. van den Brink, M. Richter, M. Prasad Ghimire, J. G. Checkelsky, and R. Comin, *Nature Materials* **19**, 163 (2020).
- [61] P. Calabrese, M. Mintchev, and E. Vicari, *Europhysics Letters* **98**, 20003 (2012).

Supplementary Material for "Computation of entanglement entropy in 2D Hubbard model: Why did we fail and how to get it right"

I. MORE DETAILS OF PROJECTOR DQMC

In this study, we focus on the calculation of the 2nd Rényi entanglement entropy S_2^A for the square lattice Hubbard model with $N = L^2$ sites. As S_2^A is a ground-state observable, the projector DQMC method is particularly suitable to compute this quantity. This method obtains the ground state $|\Psi_0\rangle$ by projecting a trial wave function $|\Psi_T\rangle$ through a relation $|\Psi_0\rangle = \lim_{\Theta \rightarrow \infty} e^{-\Theta H} |\Psi_T\rangle$, where Θ represents the projection time and H denotes the Hamiltonian of the system. And the physical observable \hat{O} is given as

$$\langle \hat{O} \rangle = \frac{\langle \Psi_0 | \hat{O} | \Psi_0 \rangle}{\langle \Psi_0 | \Psi_0 \rangle} = \lim_{\Theta \rightarrow \infty} \frac{\langle \Psi_T | e^{-\Theta H} \hat{O} e^{-\Theta H} | \Psi_T \rangle}{\langle \Psi_T | e^{-2\Theta H} | \Psi_T \rangle}. \quad (\text{S1})$$

The Hamiltonian H consists of two parts: the non-interacting $H_0 = -t \sum_{\langle ij \rangle, \sigma} (c_{i\sigma}^\dagger c_{j\sigma} + \text{H.c.})$ and the interacting $H_U = U \sum_i (n_{i,\uparrow} + n_{i,\downarrow} - 1)^2$ terms, which do not commute. We need to employ Trotter decomposition to discretize the projection length 2Θ into l_τ imaginary time slices ($2\Theta = l_\tau \Delta_\tau$) and have

$$\langle \Psi_T | e^{-2\Theta H} | \Psi_T \rangle = \langle \Psi_T | (e^{-\Delta_\tau H_0} e^{-\Delta_\tau H_U})^{l_\tau} | \Psi_T \rangle + \mathcal{O}(\Delta_\tau^2). \quad (\text{S2})$$

It is worth to note that one should set a small value for the Trotter discretization parameter Δ_τ , as the Trotter decomposition process introduces a small systematic error proportional to Δ_τ^2 .

To decouple the quartic fermionic term in H_U , we employ a SU(2) symmetric Hubbard-Stratonovich (HS) transformation at site i and time slice l_τ

$$e^{-\Delta_\tau U (n_{i,\uparrow} + n_{i,\downarrow} - 1)^2} = \frac{1}{4} \sum_{\{s_{i,l_\tau}\}} \gamma(s_{i,l_\tau}) e^{\alpha \eta(s_{i,l_\tau})(n_{i,\uparrow} + n_{i,\downarrow} - 1)} \quad (\text{S3})$$

with $\alpha = \sqrt{-\Delta_\tau U}$, $\gamma(\pm 1) = 1 + \sqrt{6}/3$, $\gamma(\pm 2) = 1 - \sqrt{6}/3$, $\eta(\pm 1) = \pm \sqrt{2(3 - \sqrt{6})}$, $\eta(\pm 2) = \pm \sqrt{2(3 + \sqrt{6})}$, which transforms the quartic term into a quadratic one. Then, we have

$$\langle \Psi_T | e^{-2\Theta H} | \Psi_T \rangle = \sum_{\{s_{i,l_\tau}\}} \left[\left(\prod_{l_\tau} \prod_i^N \gamma(s_{i,l_\tau}) e^{-\alpha \eta(s_{i,l_\tau})} \det [P^\dagger B^{s_{i,l_\tau}}(2\Theta, 0) P] \right) \right] \quad (\text{S4})$$

where P is the coefficient matrix of trial wave function $|\Psi_T\rangle$; $B^s(2\Theta, 0)$ is defined as

$$B^s(\tau_2, \tau_1) = \prod_{l_\tau=l_1+1}^{l_2} \left(e^{-\Delta_\tau H_0} \prod_i^N e^{\alpha \eta(s)(n_{i,\uparrow} + n_{i,\downarrow})} \right) \quad (\text{S5})$$

with $l_1 \Delta_\tau = \tau_1$ and $l_2 \Delta_\tau = \tau_2$, and has a property $B^s(\tau_3, \tau_1) = B^s(\tau_3, \tau_2) B^s(\tau_2, \tau_1)$. With these notations, the unnormalized weight $W^{s_{i,l_\tau}}$ of Eq. (2) in the main text could be given explicitly as

$$W^{s_{i,l_\tau}} = \gamma(s_{i,l_\tau}) e^{-\alpha \eta(s_{i,l_\tau})} \det [P^\dagger B^{s_{i,l_\tau}}(2\Theta, 0) P]. \quad (\text{S6})$$

In practice, we choose the ground state wavefunction of H_0 with as the trial wave function. The measurements are performed near $\tau = \Theta$, we set projection time $2\Theta = L$, discrete time slice $\Delta_\tau = 0.1$.

II. NON-INTERACTING LIMIT

We discuss the known results of EE in the free fermion limit $U = 0$. We choose a square region with its side of length L , and the total system size 160×160 to be closed to the thermodynamics limit. In such case, given the absence of the need for auxiliary field updates, we can directly compute the EE from Green's function matrices using Eq. (2) in the main text with $W^{s_1} = W^{s_2} = 1$. The obtained results, as shown in Fig. S1, are consistent with analytical

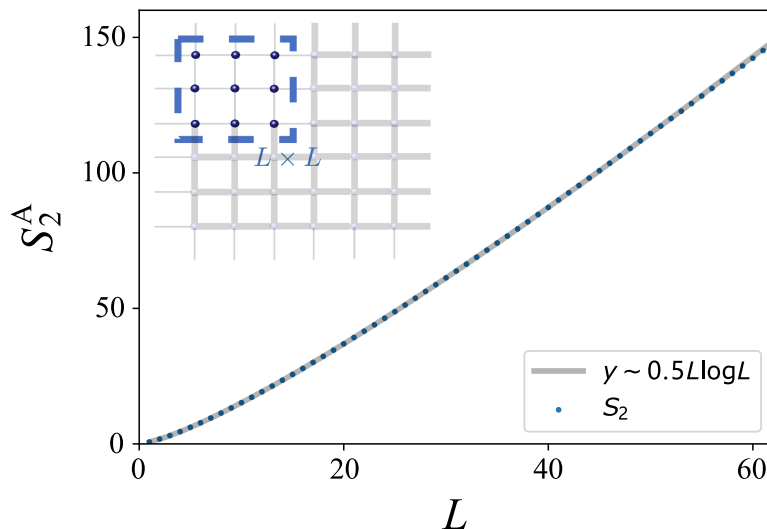


FIG. S1. The EE of the free Fermi surface on square lattice Hubbard model. The $L \log L$ scaling behavior manifests with the coefficient computed from the Widom-Sobolev formula [3–8, 12]. We choose system size 160×160 to be closed to the thermodynamics limit, and L is the length of considered square region. The grey line indicating Widom conjecture is guided by eyes. One expect $S_2 = 0.5L \log L + O(L)$.

computation from the Widom-Sobolev formula [3–8, 12], where the coefficient of the $L \log L$ term precisely governs the data. According to the formula, one has the following form of von Neumann entropy S ,

$$S^A(U=0) \sim \frac{1}{12} \frac{L^{d-1} \log L}{(2\pi)^{d-1}} \int_{\partial\Omega} \int_{\partial\Gamma} |n_x \cdot n_p| \mathbf{d}S_x \mathbf{d}S_p \quad (\text{S7})$$

where $\partial\Gamma$, $\partial\Omega$ are the boundaries of the Fermi sea and the region considered, n_p , n_x are the unit normals to these boundaries. Note $\mathbf{d}S_x$ integrates on the box region with unit length, while $\mathbf{d}S_p$ on the momentum space. The integration can be regarded as the total length of projected Fermi surface on each side of the box. Since $U=0$, we have diamond Fermi surface, which contributes 4π for one side. Finally, we have $S^A \sim \frac{4\pi \times 4}{12} \frac{1}{2\pi} L \log L = \frac{2}{3} L \log L$. Note for free system, one has the relation between von Neumann entropy and the 2nd Rényi entropy $S_2^A = \frac{3}{4} S^A$ [61]. Therefore, we expect $\frac{1}{2} L \log L$ leading term for the Rényi EE in Fig. S1. The total expression for this free limit is given in Eq. (3) where $a = \frac{1}{2}$ serves as the leading term coefficient determined by the region and Fermi surface. As shown in the grey line in Fig. S1, the $\frac{1}{2} L \log L$ curve indeed goes through the data points.

In addition, as the Fig. 3 (d) in the main text, we show the ratio $\frac{Z(\lambda_{k+1})}{Z(\lambda_k)}$ with $\lambda_k \in [0, 1]$ at the $U=0$ limit, which could be exactly computed for small system size, e.g. $L=4$. We divided λ from 0 to 1 into 50 equal slices, and plot the ratio for adjacent two λ s in Fig. S2 (a). As we expect, the ratio is closed to 1. To carefully study the distribution of the new observables for the incremental method, we plot the histogram at several λ in Fig. S2 (b). We find the distribution is almost a peak closed to $O(1)$, thus avoid the sampling problem of the direct method.

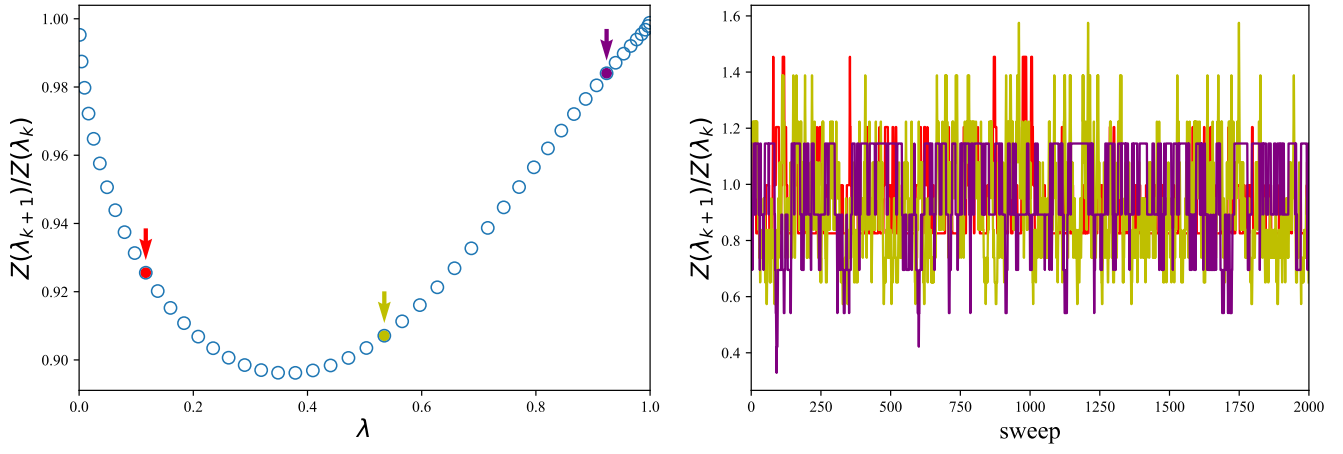


FIG. S2. (a) $\frac{Z(\lambda_{k+1})}{Z(\lambda_k)}$ for $U = 0, L = 4$ by incremental method with $\lambda \in [0, 1]$. As discussed in the main text, around Eqs. (4) and (5), each piece has the value of scale unity. Likewise in Fig. 3, the three arrows in panel(d) point out the position of three different $\lambda_k \sim 0.11, 0.53, 0.92$ values where the time series are shown in panel(b). The observables are now normal distributed.